ACS ENGINEERING Au
AN OPEN ACCESS JOURNAL OF THE AMERICAN CHEMICAL SOCIETY

pubs.acs.org/engineeringau

Article

Experimental Quantification of Gas Dispersion in 3D-Printed Logpile Structures Using a Noninvasive Infrared Transmission Technique

Leon R.S. Rosseau, Merlijn A.M.R. Schinkel, Ivo Roghair, and Martin van Sint Annaland*

Cite This: *ACS Eng. Au* 2022, 2, 236–247

Read Online

ACCESS | Metrics & More | Article Recommendations

ABSTRACT: 3D-printed catalyst structures have the potential to broaden reactor operating windows. However, the hydrodynamic aspects associated with these novel catalyst structures have not yet been quantified in detail. This work applies a recently introduced noninvasive, instantaneous, whole-field concentration measurement technique based on infrared transmission to quantify the rate of transverse gas dispersion in 3D-printed logpile structures. Twenty-two structural variations have been investigated at various operating conditions, and the measured transverse gas dispersion has been correlated to the Péclet number and the structures' porosity and feature size. It is shown that staggered configurations of these logpile structures offer significantly more tunability of the dispersion behavior compared to straight structures. The proposed correlations can be used to facilitate considerations of reactor design and operating windows.

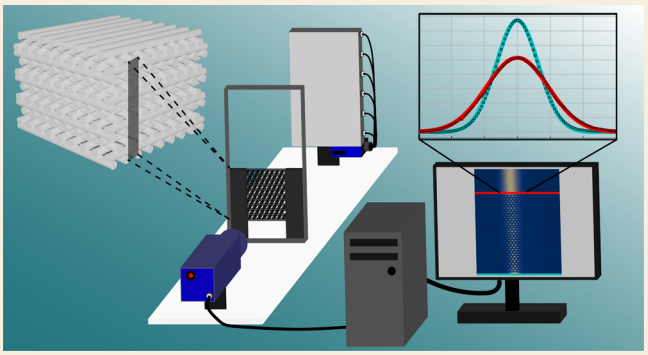

KEYWORDS: *structured reactors, 3D-printing, additive manufacturing, catalyst structuring, logpile structure, gas dispersion, infrared transmission technique*

1. INTRODUCTION

The structuring of reactor internals is commonly employed in an effort to control the gas holdup, intensify the mixing of phases, and manage the residence time distribution while maintaining a low pressure drop. In addition to this, structured catalysts aim to provide increased catalyst surface area to the reactants without compromising on process cost.[1,2] These structured catalysts, often ceramic materials, are conventionally manufactured as extrudates or through the coating of honeycomb monoliths or foams.[3] The specific geometries are optimized to manage the trade-off between good mixing, adequate temperature control, and enhanced fluid−solid contact at low pressure drop, contrasting a packed bed of pellets in which the pressure drop is relatively high and hot spots may appear.[4−6]

In the past decade, the rise of additive manufacturing (AM) technologies has allowed for the structuring of catalysts via a novel method. The additive manufacturing, or 3D-printing, of catalysts offers the potential to enable virtually infinite freedom in design and the possibility for large structures with local variations. The degree to which this promise can be fulfilled depends on the specific AM technology selected. For a thorough understanding of the different technologies, and their implications on both design freedom and chemical properties of the shaped bodies, the interested reader is referred to some of the excellent review works in this field.[7−10] In this study, structures produced through direct ink writing (DIW) will be considered. The literature on DIW features many examples of ceramic-like catalysts, such as zeolites and metal−organic framework materials, and catalyst support materials such as silica and alumina, being 3D-printed, and it is arguably the most mature technology in this context.[11] For DIW, a viscous slurry of catalyst particles, binder materials, and a diluent is prepared. This slurry is extruded through a circular nozzle as it follows a programmed pattern along a print surface, thus laying down and stacking cylindrical features.[12,13] Most studies in the literature use this method to produce monolith-like logpile structures in either a straight or a staggered configuration, where the placement of features in the axial direction is either parallel to or offset from the previous layer. The geometry of such structures is varied by changing the size of the printed features and the relative size of the aperture between them to tailor the porosity.[14] In an effort to ensure that the printed structure has adequate mechanical strength, the intended porosity, and no loss of catalytic activity, researchers have

Received: December 23, 2021
Revised: March 2, 2022
Accepted: March 2, 2022
Published: May 2, 2022

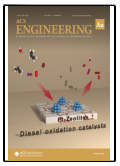

optimized critical parameters in the printing process, such as printer settings, rheological properties of the slurry, and postprocessing protocols.[15,16] While these are all vital aspects of the shaping of the catalytic material, the reactor-scale implications of the geometry are often underexposed.

The proposed logpile structures would allow reactants to travel in the transverse direction, which is implied by the alternate stacking of features during printing, and this discerns them from conventional honeycomb monoliths. This transverse mixing may enable broader operating windows, and possibly better heat transfer from the walls to the center of the reactor; a well-known downside of ceramic honeycomb monoliths when scaling up.[17] Enhanced heat transfer due to increased transverse dispersion may benefit chemical processes by decreasing the hot spot temperature for reaction systems with strong heat effects, decreasing the risk of thermal runaway and material degradation. This also improves the performance, as adequate temperature control suppresses side-reactions which decrease the selectivity toward the desired product.[4,18] In addition, the relatively poor transverse heat transfer of conventional packed bed reactors necessitates the use of reactor tubes with a small diameter in order to supply a sufficient heat exchange area, which brings along increased pressure drop and complications in distributing reactants evenly over the various tubes. Better thermal management thus allows using tubes with a larger diameter and decreases the operational costs for compressors.[19] The postulated potential depends largely on the extent of transverse dispersion that can be achieved and on the tailoring of this parameter by changing the design of the structure. Since quantitative information on the transverse dispersion is not yet available, this study aims to establish the relationship between the extent of gas dispersion and structural design parameters for different configurations of 3D-printed logpile structures.

Diffusion and dispersion phenomena are commonly assessed through the use of a tracer injected from a continuous point source. Alternatively, an object made of soluble tracer material may also be immersed in the flow. Through different analytical techniques, such as spectrophotometry or conductivity measurements, the concentration of the tracer component can be mapped as a function of the downstream position.[20,21] This information is then used to determine the transverse dispersion coefficient. Such measurement techniques require multiple, possibly invasive, measurement probes to obtain a representative concentration profile that can be processed to yield the transverse dispersion coefficient. More sophisticated experimental techniques are also available, for example employing magnetic resonance techniques to investigate the flow field. While such techniques are relatively complex and require expensive equipment, the whole field can be studied in a noninvasive manner, which has considerable benefits.[22,23] In recent years, the increasing computational power of modern computers has been used to eliminate the need for traditional experiments and obtain hydrodynamic properties of reactors through detailed computational fluid dynamics studies.[24,25] It remains, however, computationally expensive to perform full-scale simulations of complex geometries.

In this study, a recently introduced noninvasive, instantaneous, whole-field concentration measurement technique based on infrared (IR) transmission is employed to quantify the transverse dispersion in 3D-printed logpile structures. This method uses a setup featuring an IR source and a pseudo-2D column through which an IR-absorbing tracer gas is fed. By the use of an appropriately configured IR camera, the visualization of tracer gas flow through the 3D-printed structure is enabled.[26,27] Combining this with quantitative knowledge on the relationship between absorbance by the tracer gas and its concentration allows for the quantitative description of concentration profiles throughout the column. The fact that the entire concentration field is determined within a single measurement offers significant advantages over conventional methods that require individual, possibly invasive, measurement probes for each downstream position. In addition, visualization of the whole field allows for the identification of phenomena beyond dispersion, such as stagnant zones.

Since the methodology has not been used for this purpose yet, its working principles and the required numerical treatment of the data are first introduced and later validated. The validated method is then used to assess the transverse dispersion coefficient of twenty-two logpile structures of various configurations at different superficial velocities. The results are used to develop a correlation relating the superficial velocity and geometrical properties of the structure to the observed transverse dispersion. An analysis of the statistical relevance of these results and the correlation is presented as well.

2. METHODS

2.1. Experimental Setup

The experimental setup consists of an IR source, a pseudo-2D column, and an IR camera, all located in a climate controlled box. The setup is shown in Figure 1.

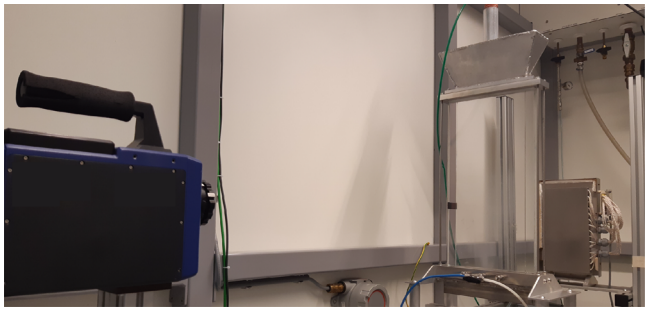

Figure 1. Experimental setup consisting of the IR source on the right, quartz glass column in the middle, and IR camera on the left.

The IR source is an anodized aluminum plate of 15 cm by 30 cm which is heated to 430 °C by electrical tracing wires. Even spacing of these wires and proper insulation allow for a stable temperature of the plate during the experiments.

The structure under study is held in a flat column of 20 cm wide and 50 cm high, with a gap of slightly less than 4 mm and equipped with a thermocouple to monitor the temperature. The column features a porous distributor at the bottom through which nitrogen is fed as background gas. Just above this distributor plate, an injector is located through which tracer gas is fed. In this configuration, the tracer is injected perpendicularly to the nitrogen flow, which does not constitute a perfect point source. To account for this, the flow is allowed to stabilize in an inlet zone of about 10 cm before entering the structure. Previous work by our group has employed sapphire as a column material because of its excellent IR transmissive properties over a broad range of wavelengths, which allowed CO_2 to be used as a tracer gas (with a characteristic absorption peak at 4.26 μm).[26] However, this material is not fit for the production of larger columns, in part due to its high cost. In an effort to scale up the technique, subsequent work by our group has shown that quartz glass is a

https://doi.org/10.1021/acsengineeringau.1c00040
ACS Eng. Au 2022, 2, 236−247

suitable material as long as the characteristic absorption peak of the tracer gas is less than 3.5 μm. To meet this constraint, propane was used as tracer gas (with a characteristic absorption peak at 3.46 μm).[27] The combination of quartz glass as column material and propane as tracer gas will also be used in this study.

The final element of the setup is a FLIR SC7650 IR camera. The camera has a spectral range from 1.5 to 5.1 μm, an aperture size of f/2.5, a resolution of 640 by 512 pixels and a maximum frame rate of 100 Hz. The camera is equipped with a mechanical filter wheel, in which a sapphire band-pass filter with a center wavelength of 3.46 μm and a transmission of 80% is mounted (Edmund optics).

All elements are placed on a skid and oriented such that they are parallel, minimizing the effects of reflection and refraction. The distance from the camera to the column has been varied in an effort to minimize the Narcissus effect (distortion of the image due to self-reflection of the camera system) and optimize the field of view while retaining adequate contrast.[28] The main considerations in optimizing the field of view are to ensure that the whole structure is captured in the IR source and that enough space is present at both the bottom and top of the structure to visualize the inflow and outflow zones. In the final configuration, the captured field of view is approximately 17 cm wide and 14 cm high; one pixel length is equal to 270 μm. The movement of the camera relative to the IR source does imply that the integration time should be adjusted to provide optimal contrast and avoid oversaturation of the detector.[27] In this work, it was established that an integration time of 750 μs provided optimal contrast.

2.2. 3D-Printed Structure

For the purpose of this study, plastic structures will be used rather than actual 3D-printed catalyst structures. This is done since the assessment of dispersion does not require any catalytic activity, and since the shaping of polymers via additive manufacturing is faster and cheaper compared to the printing of ceramic powders.[29] In addition, the samples obtained after 3D-printing and calcining of catalyst powders are typically quite brittle, and it would be fairly difficult to seal these structures to an adequate degree for the current purpose.[8,30]

All the structures in this work were designed in Blender, sliced for printing in PrusaSlic3r, and printed on a Prusa MK3S fused deposition modeling (FDM) machine. Poly(lactic acid) was used as a printing polymer, since it is readily available and easy with which to print. This material is also opaque to the IR camera at the current settings, which is beneficial for obtaining images that are well focused.[31]

The direct ink writing of catalytic logpile structures yields cylindrical features which originate from a circular nozzle. Contrasting this is polymeric fused deposition modeling, in which the plastic is squished from the nozzle onto the print surface and hence, any round feature has to be constructed from layers, producing the so-called staircase effect.[32] This limits the resolution of print features and through trial-and-error, it was assessed that cylindrical features ranging from 1.2 mm to 2.0 mm diameter can be printed with an adequate resolution, using a nozzle of 0.25 mm in diameter. In the literature, logpile structures produced via DIW commonly have a feature size on the order of hundreds of micrometers, but efforts employing a feature size of 1.5 mm are reported as well.[14,33] Hence, the feature size of FDM-produced structures in this study is in line with the DIW counterpart in the literature, if not slightly on the high end. The stepped surface of printed features may introduce surface roughness that is not present in (ceramic) catalytic structures, but the effect of this on the transverse dispersion behavior is considered to be negligible. Another artifact from DIW that has to be reproduced is the slight sagging of features in the axial direction. As features are stacked, they dent the previous layer and this can be described by an axial stacking offset of approximately 80% of the feature size. This factor was determined from visual assessment of printed structures.[14,34]

A visualization of this structure, along with relevant dimensions, is shown in Figure 2. All printed structures have a size of 8 cm by 10 cm. The third dimension is required to support the features, and consists of two half cylinders of 1.5 mm diameter on either side, with an aperture of 1.5 mm in the middle. This effectively replicates the third

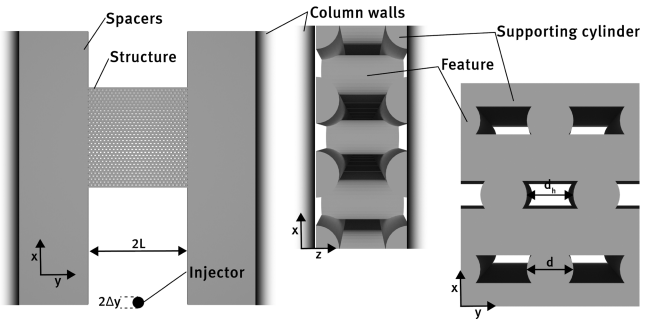

Figure 2. Visualization of the 3D-printed structure and relevant dimensions, with the full structure and spacers shown on the left, a detailed side view in the middle, and a detailed front view on the right. Column walls are sketched to illustrate structure placement inside of the column.

dimension of actual structures and ensures a tight fit in the column. However, it should be noted that the fixed thickness may introduce some pseudo-2D effects when the feature size is not equal to 1.5 mm. Additionally, while the third dimension is indeed replicated for a single repeating unit, the presence of the column walls introduces a pseudo-2D inconsistency as their no-slip boundary does not correspond to the actual situation in which fluid is free to travel in this direction. Spacers are placed on either side of the structure to center it and ensure that every tested structure has the same relative position. Additionally, spacers are fitted on the bottom to allow for an inlet zone.

The structures to be tested have variations in feature size (from 1.2 mm to 2 mm), configuration (straight or staggered), and porosity. The porosity is varied by changing the size of the aperture between the features. In Table 1, all variations investigated in this work are tabulated. Each of these variations is tested twice, in either the staggered or the straight configuration.

Table 1. Relevant Parameters of the Structures That Have Been Tested in This Work

d[mm]	d_h[mm]	ϵ[−]
1.5	0.75	45.1%
1.5	1.0	48.1%
1.5	1.5	52.7%
1.5	2.0	55.9%
1.5	3.0	60.3%
1.2	0.6	41.8%
1.2	1.2	48.7%
1.2	1.8	52.8%
2.0	2.0	57.4%
2.0	3.0	62.2%
2.0	4.0	65.4%

For validation purposes, the measurements were also conducted with a packed bed of spheres with a diameter of 2.5 mm. To enable this experiment, a 3D-printed distributor plate was produced to support the packed bed at the intended height and allow for the required inlet zone. By measuring the weight of the bed, and using the density of the particles, the porosity was determined to be 57% and 62% upon repacking. This is rather high for a packed bed, which generally attains values between 36 and 40%, but this can be explained by the pseudo-2D nature of the experiment and the high ratio of particle size to column depth.

2.3. Experimental Section

First, a structure is installed into the column and the IR source is turned on. The setup is then left to stabilize for 3 h. This time allows the whole setup to be in thermal equilibrium so that external

https://doi.org/10.1021/acsengineeringau.1c00040
ACS Eng. Au 2022, 2, 236−247

fluctuations during experiments are minimized.[27] Next, the feed rates of tracer gas and nitrogen are set, and the camera records 120 images with a frequency of 1 Hz. For every structure, the feed rate of nitrogen is varied between 1.90 L min^{-1} and 19.2 L min^{-1}, corresponding to a superficial velocity between 0.10 m s^{-1} and 1 m s^{-1}. The flow rate of propane is fixed at 0.12 L min^{-1}, the lowest value that can stably be achieved by the mass flow controller used. A low value ensures that the inlet flow field is not disturbed greatly.

The obtained images contain the infrared intensity values per pixel. This can be converted to the transmission (eq 1) and in turn, the absorbance (eq 2), by using a background image. The background image is recorded without propane flow, and serves to take into account the local inhomogeneities throughout the infrared source.

$$T = \frac{I}{I_0} \tag{1}$$

$$A = -\log_{10}(T) \tag{2}$$

2.4. Calibration

Before gas dispersion coefficients can be determined, a quantitative relationship between the absorption of infrared radiation by the tracer gas and its concentration needs to be established. To this end, a series of experiments is conducted with mixtures of nitrogen and propane in fixed ratios. Both gases are mixed prior to entering the column via the porous distributor for these experiments. The dependency between concentration and the degree of IR absorption is often described as linear. However, in previous work by our group it was noticed that over a broad concentration range, the linear approach does not suffice anymore and a polynomial description is required.[27,28] Fitting this curve to the experimental data is done with the SciPy curve_fit tool in Python 3.7.4. This tool will also be used in subsequent fitting operations. The global calibration curve, composed by averaging all pixels, is displayed in Figure 3. Owing to small inhomogeneities in the IR source, the standard deviation of this curve is relatively high, as indicated by the error bars in Figure 3. To account for this effect, pixel-based calibration curves are employed. The fitting procedure is the same, but it is automated and generates arrays of the polynomial coefficients.

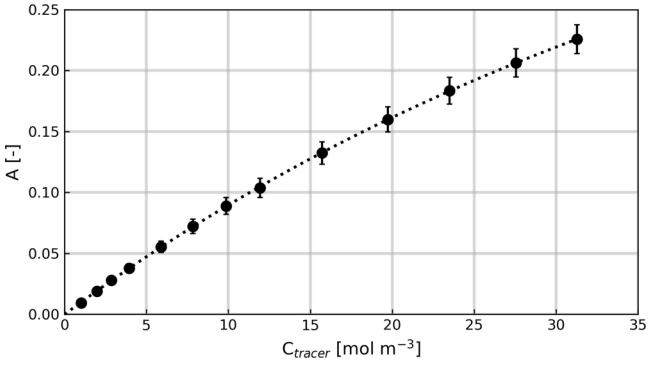

Figure 3. Calibration data with standard deviation (dots) and fitted curve (dotted line).

3. DATA EVALUATION

The ability to visualize and determine concentrations of gases is used to determine the transverse dispersion coefficient of different 3D-printed structures. The plume of tracer gas that is injected is expected to travel upward through the column and spread due to dispersion and diffusion. This situation is expressed in a general manner through the unsteady convection−diffusion equation for the tracer, eq 3.

$$\frac{\partial C}{\partial t} = \nabla\cdot(D\nabla C) - \nabla\cdot(\mathbf{u}C) \tag{3}$$

Finding a position-dependent solution to this equation in the current form requires advanced numerical techniques. It is, however, possible to simplify the equation using the following assumptions:

- The system is at steady state. Any small fluctuations will be eliminated by time-averaging multiple images.
- The convection is only directed upward, in the positive x-direction, and any influence of y- or z-dependent velocity profiles due to the presence of the 3D printed structure is lumped into the dispersion coefficient. The axial velocity profile is uniform;
- The dispersion is only directed into the y-direction. Any influence of mass transport in the z-direction (the depth direction) is lumped into the dispersion coefficient in the spirit of the pseudo-2D character of the experiment. This assumption introduces a dependency on the column thickness, as this thickness determines the relative influence of the no-slip boundaries on the front and back walls. Further discussion on this influence will be given in the Results section. Additionally, the influence of axial dispersion is considered to be negligible in the current experiments, which is valid at high Péclet numbers.
- The dispersion coefficient is assumed to be constant. This is allowed since there are no local variations in the structure and since the temperature in the column is relatively constant. This also holds for the velocity, but a small disturbance in velocity profile may arise when the tracer is injected at a largely different velocity than the background gas.

Applying these assumptions yields eq 4 (with u representing the interstitial axial velocity and D_t the transverse dispersion coefficient).

$$u\frac{\partial C}{\partial x} = D_t\frac{\partial^2 C}{\partial y^2} \tag{4}$$

Table 2 shows the boundary conditions that are applicable to the situation of a tracer source of fixed width and an imposed concentration that is injected into a domain with a fixed width. Using these boundary conditions, the partial differential equation (eq 4) can be solved, yielding an analytical expression (eq 5) for the concentration of tracer as a function of position.[35] The corresponding standard deviation is shown in eq 6.

Table 2. Boundary Conditions for the Convection-Diffusion Equation with a Column Width of 2L and an Injector Width of 2Δy

$x = 0$	$-\Delta y \le y \le \Delta y$	$C = C_0$
$x = 0$	$-L \le y < -\Delta y \wedge \Delta y < y \le L$	$C = 0$
$x > 0$	$y = -L \wedge y = 0 \wedge y = L$	$\partial C/\partial y = 0$
$x \to \infty$	$-L < y < L$	$C = (\Delta y/L)C_0$

https://doi.org/10.1021/acsengineeringau.1c00040
ACS Eng. Au 2022, 2, 236−247

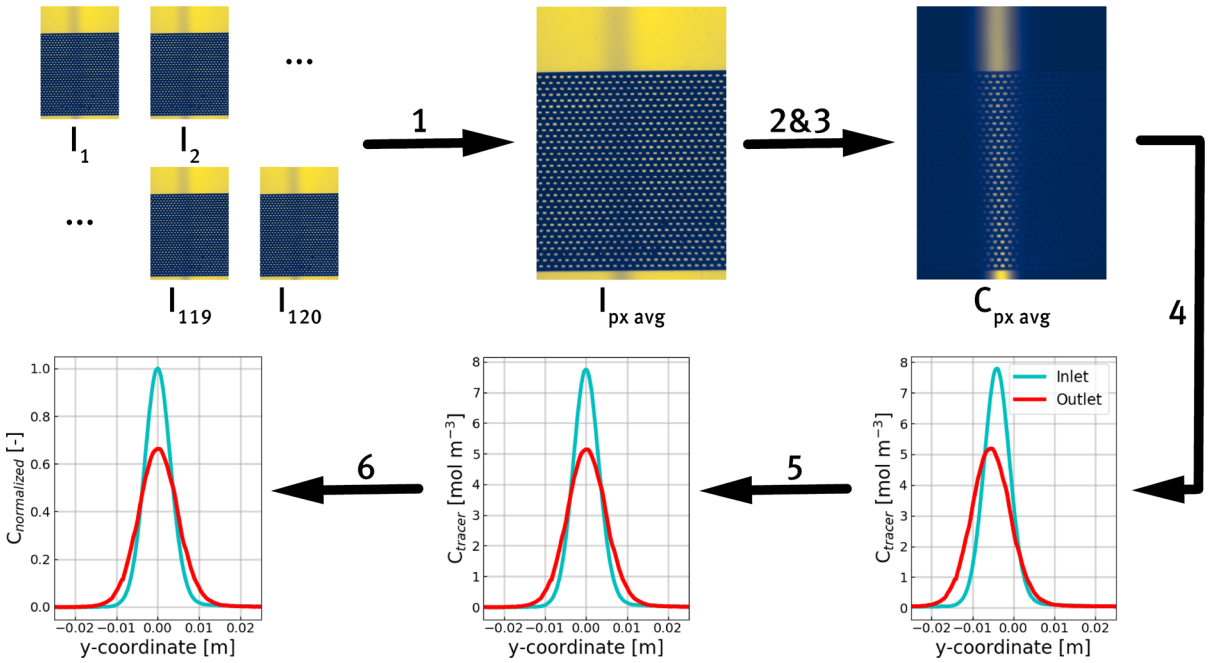

Figure 4. Visual representation of the data preparation procedure, with the different steps: (1) element-wise averaging of the images; (2) conversion of intensity to absorbance; (3) conversion of absorbance to tracer concentration; (4) extracting the inlet and outlet of the structure; (5) peak centering and baseline correction; (6) peak normalization.

$$C = \frac{C_0}{2}\sum_{n=-\infty}^{\infty}\left(\mathrm{erf}\left(\frac{\Delta y - 2nL + y}{\sigma\sqrt{2}}\right) + \mathrm{erf}\left(\frac{\Delta y + 2nL - y}{\sigma\sqrt{2}}\right)\right) \quad (5)$$

$$\sigma = \sqrt{\frac{2D_t x}{u}} \quad (6)$$

The derived equation and the used pseudo-2D approximation in this study imply that the 2D molar flux has the unit mol m^{-1} s^{-1}, and is obtained by multiplying the molar flux by the column depth. The 2D molar flux is used to determine C_0 and Δy.

3.1. Preparing the Data for Fitting

The obtained data consist of images, in which each pixel has an intensity value which can be correlated to a tracer concentration, as described in the previous calibration subsection. The data are prepared for fitting according to the following routine, which is visualized in Figure 4.

1. Element-wise averaging of the images. To obtain a representative image, the final image is constructed by averaging 120 images obtained with a frequency of 1 Hz.
2. Conversion of intensity to transmittance by element-wise division of the image under study by the background image and subsequent conversion to the absorbance.
3. Conversion of the absorbance to the concentration of tracer by element-wise application of the calibration curve.
4. Extracting the inlet and the outlet of the structure. This is done by determining the relative height of the structure inlet and outlet in terms of pixel positions. The values along the y-coordinate at these x-coordinates are then stored.
5. Peak centering and baseline correction. The maximum concentration at each x-coordinate is taken, and the index of this value is set to be the origin on the y-coordinate. The data are then corrected by a baseline constructed by averaging the outer 5% of the values.
6. Peak normalization. It was noticed experimentally that the camera struggles to identify the very lowest propane concentrations, and hence, it appeared as if some mass was lost at higher axial positions. This is accounted for by normalizing the peak. For normalization, the fictitious injector width is adjusted to correspond to the molar flux that is represented by the area of the peak.

3.2. Fitting the Dispersion Coefficient

It was mentioned that the structure is placed higher than the injection point and therefore, the tracer has had the opportunity to spread. This does not comply with the assumption of a well-defined tracer source with uniform concentration, as described by the boundary conditions in Table 2. To account for this, a fitted reference value is used which includes the effects of the nonperfect tracer source as well as the development of the velocity profile in the inlet zone. This value is obtained by solving eq 5 for the reference standard deviation (σ) at the inlet. Using the fitted inlet value, the spreading of the tracer due to the structure can be decoupled by considering eq 7. The transverse dispersion coefficient is calculated via eq 8, using the superficial gas velocity (U) and the average gas holdup in the structure (ϵ).

$$\sigma_{\mathrm{outlet}} = \sqrt{\sigma_{\mathrm{inlet}}^2 + \sigma_{\mathrm{structure}}^2} \quad (7)$$

$$D_{\mathrm{structure}} = \frac{\sigma_{\mathrm{structure}}^2 u}{2x} = \frac{(\sigma_{\mathrm{outlet}}^2 - \sigma_{\mathrm{inlet}}^2)U}{2x\epsilon} \quad (8)$$

The relative height of the structure is calculated by multiplying the number of pixels between the reference height and the height of the outlet and multiplying this by the size of one pixel

https://doi.org/10.1021/acsengineeringau.1c00040
ACS Eng. Au 2022, 2, 236−247

(h.l. 270 μm). An example of an infrared image and the fitted inlet and outlet concentration profiles is shown in Figure 5.

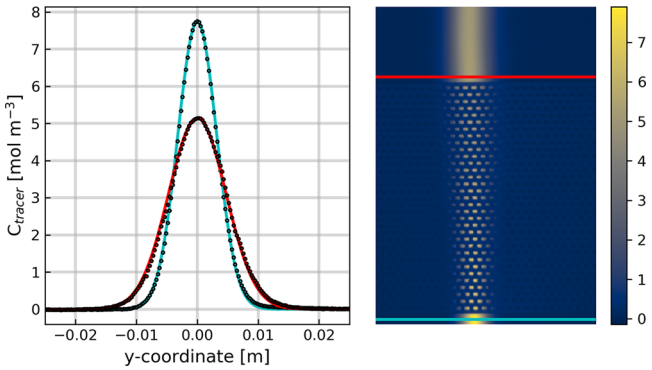

Figure 5. Inlet and outlet concentration profiles after the data processing and fitting procedure, with dots as experimental data on the left-hand side. The image from which this data is extracted, with horizontal lines indicating the inlet and outlet is shown on the right-hand side. The structure shown has a staggered configuration, a feature size of 1.5 mm and a porosity of 52.7%. The experiment was conducted at a superficial velocity of 0.31 m s^{-1}.

3.3. Correlating the Dispersion Behavior

To enable exploitation of the results beyond the current work, an attempt will be made to correlate the extent of transverse dispersion to the operating conditions and the porosity and configuration of the structure, commonly in the form of the dimensionless transverse Péclet number. The Péclet number for molecular diffusion equals the product of the Reynolds number (Re, eq 9) and the Schmidt number (Sc, eq 10), divided by the porosity of the structure, as shown in eq 11. For packed columns, a correlation is usually proposed in the form of eq 12, with the generally accepted form for gas-phase systems in packed beds of spheres shown in eq 13.[20,36] The factor τ represents the tortuosity, which has a value of $\sqrt{2}$ in a randomly packed bed of spheres. The dispersion behavior of fluids with higher Schmidt numbers in packed beds is more complex, and several conditional correlations are required to describe the entire range of Reynolds numbers.[37−39]

$$Re = \frac{\rho U d}{\eta} \tag{9}$$

$$Sc = \frac{\eta}{\rho D_m} \tag{10}$$

$$Pe_m = \frac{ReSc}{\epsilon} = \frac{ud}{D_m} \tag{11}$$

$$\frac{D_t}{D_m} = \alpha + \beta Pe_m^{\gamma} \tag{12}$$

$$\frac{D_t}{D_m} = \frac{1}{\tau} + \frac{1}{12} Pe_m \tag{13}$$

The data gathered in this work will be used to propose a correlation in the form of eq 12 to describe the transverse dispersion in logpile structures. To be able to quantify the statistical relevance of such a correlation, the mean absolute percentage error (MAPE) is used, defined in eq 14 (where D_t is the experimental value and $\bar{D}_t$ is the fitted value).

$$\text{MAPE} = \frac{1}{N} \sum_{n=1}^{N} \left| \frac{D_t - \bar{D}_t}{D_t} \right| \tag{14}$$

4. RESULTS

4.1. Validation of Molecular Diffusion Coefficient

The novel methodology will first be validated by conducting experiments in an empty column, as these calculations should yield the molecular diffusion coefficient. The average temperature in these experiments was 32 °C, corresponding to a diffusion coefficient of propane in nitrogen of 1.18 × 10^{-5} m^2 s^{-1}.[40] The superficial velocity was varied, and the experimental diffusion coefficient was determined at every axial position. These 340 values were then averaged, and the standard deviation was calculated to verify that the axial variation of calculated values is minimal. The results are shown in Figure 6.

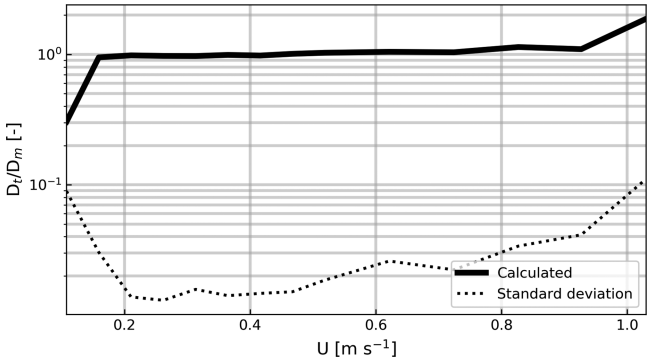

Figure 6. Validation of the measurement of the molecular diffusion coefficient in an empty column. Values were averaged over 340 positions along the axial coordinate, and the standard deviation was calculated from this data.

The majority of the data in Figure 6 is very close to the value reported in the literature, and at approximately 2%, the coefficient of variation is also low for these points. On either side of the graph, a larger deviation can be observed. At low velocities, this can be explained by the fact that the tracer plume is so broad that a representative baseline cannot be well established. On the other hand, at high velocities the spreading of the tracer plume is limited and hence the resolution of the image becomes limiting. This latter phenomenon is exacerbated by the relatively small field of view used. At the highest velocities, the gas stream travels through the field of view (approximately 10 cm) so quickly that only a very small amount of diffusion takes place. It could be hypothesized that in addition to this, turbulent effects may influence the apparent diffusion coefficient at higher velocities. However, at the highest velocity tested the Reynolds number based on the column depth is equal to 244, indicating laminar flow. With these effects in mind, it can be concluded that the setup is validated for use with moderate gas velocities, from 0.15 m s^{-1} to 0.7 m s^{-1}. In addition, the calculated standard deviations are deemed quite acceptable, taking into account the spread in literature data as well as the accuracy of the mass flow controllers.[40−42]

4.2. Validation of Transverse Dispersion in a Packed Bed

The current experimental method was then used to determine the transverse dispersion in a packed bed of spheres. This can be used for validation, as correlations are available from the

https://doi.org/10.1021/acsengineeringau.1c00040
ACS Eng. Au 2022, 2, 236−247

literature for comparison. The spreading of the tracer plume by the distributor and the inlet zone was decoupled from the dispersion caused by the packed bed. This is done by extending eq 8 to account for the dispersion induced by the distributor (eq 15), and performing a separate experiment with only the distributor in place to determine $\sigma_{distributor}$. The results of this validation, performed in duplicate, are summarized in Figure 7.

$$D_{PB} = \frac{\sigma_{PB}^2 u}{2x} = \frac{(\sigma^2 - \sigma_{inlet}^2 - \sigma_{distributor}^2)U}{2x\epsilon_{PB}} \quad (15)$$

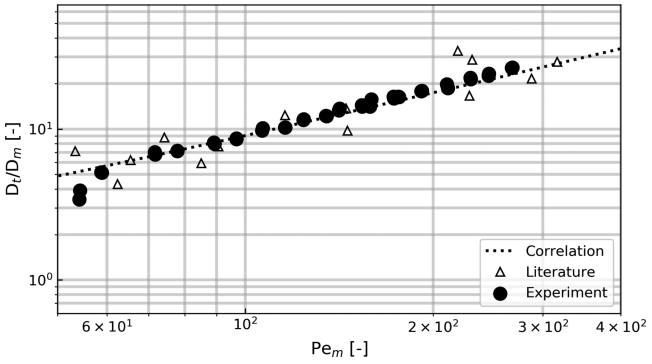

Figure 7. Validation of packed bed relative transverse dispersion with spheres of 2.5 mm. Each experimental data point was collected in duplicate and these points almost completely overlap. The correlation for transverse dispersion in gas phase systems, eq 13, is plotted with $\tau = \sqrt{2}$ alongside literature data taken from Coelho and Guedes de Carvalho.[43]

It is seen in Figure 7 that the experiments are very reproducible as the data points from duplicate experiments are almost completely overlapping and thus there seems to be little influence of the packing (note that the structure porosity was taken into account). In addition to this, the correspondence between the experimental data and the correlation is very good with a MAPE of only 6.83%, especially when taking into account the correlations' reported standard deviation of 12%.[37] At lower Péclet numbers a somewhat larger deviation is observed, but this is likely due to the same effects that were present in the validation of the molecular diffusion coefficient. Hence, the novel experimental method is hereby validated to be an accurate alternative to conventional methods to measure transverse dispersion, and can subsequently be used to quantify the transverse dispersion in 3D-printed logpile structures.

4.3. Reproducibility of Logpile Structure Measurements

The excellent reproducibility of the validation measurements was already shown, but to allow for proper data interpretation, it is important to verify that this also holds for the measurements with 3D-printed logpile structures. To this end, measurements were conducted in triplicate or in quadruplicate. For the staggered structures, 2 of the 11 structures were measured in triplicate, and this yielded an average coefficient of variation of 1.88%, being in accordance with the significance of the validation cases. For the straight structures, however, an average coefficient of variation of 10.9% was found when considering a structure measured in triplicate and another measured in quadruplicate.

To elucidate the origin of the relatively poor reproducibility for straight structures, the outlet tracer concentration profiles of a straight structure and its staggered counterpart are compared in Figure 8. The staggered data are, as expected, very similar. For the straight structures, however, larger deviations are observed, and it can be seen that the profiles are not as smooth as expected. The small bumps in the experimental concentration profile are likely a result of the structure-induced velocity profile, which is channeled for straight structures (in contrast to the more uniform velocity distribution that can be expected from a staggered configuration). It is reasonable to assume that this leads to a decrease in the quality of fit as the condition of a uniform velocity profile is not satisfied. In addition, the reproducibility is further decreased by deviations between experiments due to the channeled structure. More specifically, a slight offset in structure placement may change the relative location of the injection and influence the spreading of tracer through the structure to a disproportionate degree. A final origin of the poor reproducibility could be small fluctuations in the gas supply between experiments, which are likely dampened out in the staggered structures, but enhanced in the straight configuration due to the channeling.

An option to improve the relatively poor reproducibility of the straight structure data would be to include an outflow region. Additional dispersion in the outflow region would then

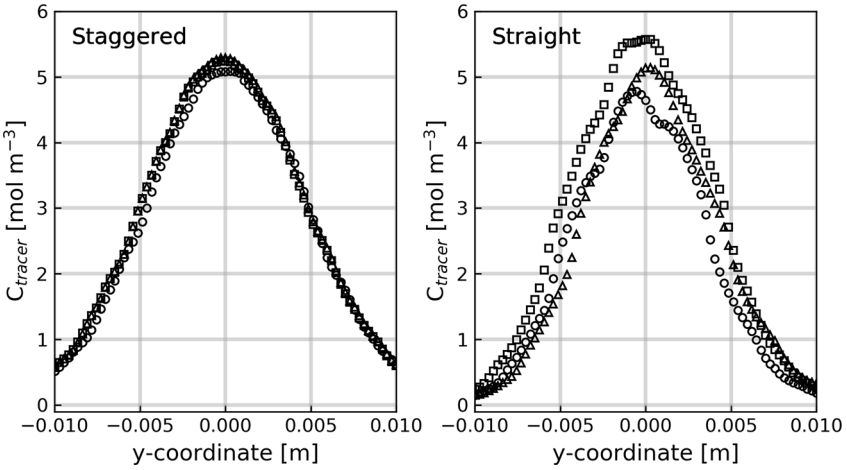

Figure 8. Comparison of outlet tracer concentration profiles of a staggered (left) and a straight (right) structure, both experiments with 1.5 mm feature size, a porosity of 52.7%, and a superficial velocity of 0.31 m s^{-1}. Different markers represent triplicate experiments.

https://doi.org/10.1021/acsengineeringau.1c00040
ACS Eng. Au 2022, 2, 236−247

be characterized by the superficial velocity and the molecular diffusion coefficient. This approach was tested for the packed bed validation case, but it was observed that the outflow zone requires more careful consideration. This is likely due to a initial settling zone in which the velocity profile needs to develop. The hydrodynamics involved in the development within this zone are complex and would require intricate modeling which is beyond the scope of the current work. Hence, this option is abandoned, and the relatively high variability of the straight structure data should be kept in mind.

4.4. Transverse Dispersion in Logpile Structures

In this study, 11 different structural variations were tested in both staggered and straight configurations. First, the data of the structures with a feature size of 1.5 mm are considered. These structures are exempt from possible pseudo-2D effects as both the features and supporting cylinders are of the same size. Five different porosities were investigated, and the results are shown in Figures 9 and 10 for the staggered and straight configurations, respectively.

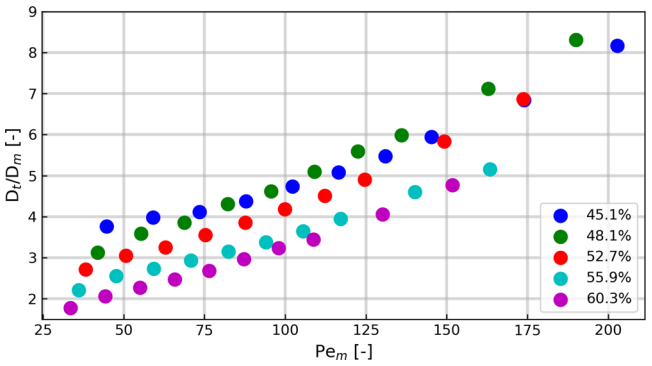

Figure 9. Experimental data of the relative transverse dispersion in different staggered structures with 1.5 mm feature size and varying porosity.

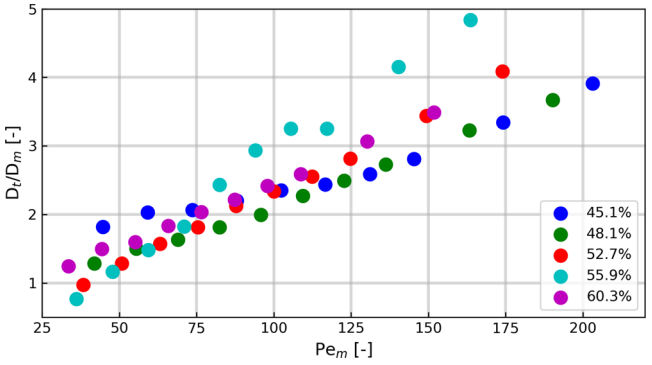

Figure 10. Experimental data of the relative transverse dispersion in different straight structures with 1.5 mm feature size and varying porosity.

When comparing the staggered and straight structure data, it is observed that the transverse dispersion is significantly lower for the latter configuration, especially at higher Péclet numbers. This can be attributed to the channeled, monolith-like, geometry of the straight structures, which limits the degree of transverse dispersion. This is contrasted by the staggered structures, where the flow is constantly split as it navigates the tortuous path around the cylinders, thereby enhancing the lateral mixing. In addition, it can be observed that for a staggered structure the relative transverse dispersion coefficient is a function of the porosity (see Figure 9). This enables tunable dispersion behavior by modification of the structures' geometry, which is one of the major advantages of 3D-printed logpile structures in comparison to randomly packed beds. The general trend is that the transverse dispersion increases as the porosity decreases. This may be expected for this configuration, as a lower porosity represents the situation in which the cylinders are closer together, and thus the path for the flow is more tortuous. In contrast, for a higher porosity, the ratio between aperture size and cylinder diameter is larger than one and small channels emerge, decreasing the amount of transverse dispersion. Exceptions to this trend are also observed though, for example, where the curves of 45.1% and 48.1% switch order in the graph at higher Péclet numbers. This suggests that a more complex dependency on the porosity is likely present. In contrast, for the straight structures, it is observed in Figure 10 that the dependency on the porosity is not very pronounced and the differences in relative transverse dispersion are rather small, particularly at lower Péclet numbers (especially when considering the higher standard deviation of the data for the straight structures). Hence, the straight configuration fulfills the potential of the 3D-printing technology to a lesser degree. The channeled flow through the straight structure limits the transverse dispersion and only at higher Péclet numbers can some effect of the structures' porosity be observed. This is probably related to the increased mixing for flow past cylinders at higher Reynolds numbers, because of the increased distance between cylinders for structures of higher porosity.

Finally, it can be observed that for straight structures, the transverse dispersion increases linearly with the Péclet number, similarly to packed beds of spheres, whereas the transverse dispersion increases superlinearly as a function of Pe_m for the staggered configuration. This can again likely be related to the enhanced mixing for flow past cylinders at higher Reynolds numbers because of the increased space between the features in comparison to a packed bed of spheres.

The results of the experiments with feature sizes of 1.2 mm and 2 mm are shown in Figures 11 and 12, for the staggered and straight configurations, respectively.

As mentioned, these results may be influenced by pseudo-2D effects as features and supporting cylinders are not of the same size. It is indeed observed that the trends of these alternate feature sizes do not exactly follow the general

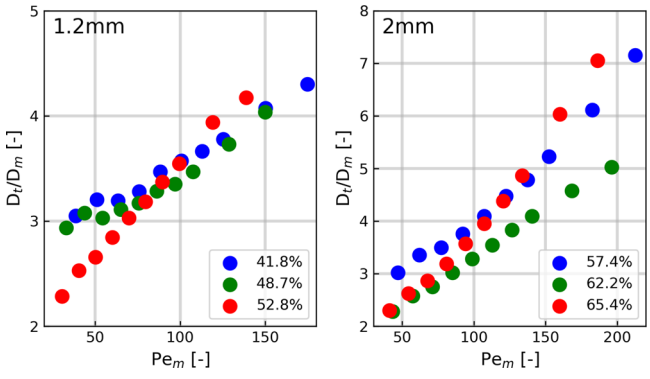

Figure 11. Experimental data of the relative transverse dispersion in staggered structures with varying porosity and a feature size of 1.2 mm (left) or 2 mm (right).

https://doi.org/10.1021/acsengineeringau.1c00040
ACS Eng. Au 2022, 2, 236−247

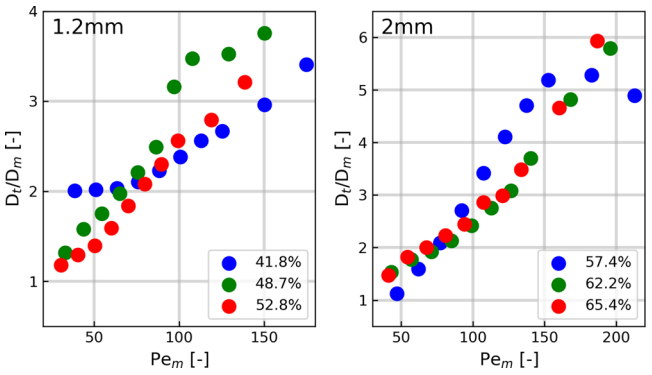

Figure 12. Experimental data of the relative transverse dispersion in straight structures with varying porosity and a feature size of 1.2 mm (left) or 2 mm (right).

conclusions of the 1.5 mm structure data. In general, none of the results exhibit a clear dependency on the porosity as was the case in Figure 9, and the transverse dispersion is less different for structures of different porosity, as was the case in Figure 10. For the staggered configuration, it can be observed that at low Péclet numbers, the relative transverse dispersion is approximately equal for the different structural variations (see Figure 11). At higher Péclet numbers, the relative transverse dispersion of the structures with 2 mm feature size increases more strongly compared to the structures with 1.2 mm feature size. It could be hypothesized that larger cylinders create a higher mixing intensity in their wake, but the current data would need to be supplemented with modeling studies to elucidate whether this is the case. For the straight configuration, the general trends in Figure 12 are better in accordance with the original results in Figure 10 compared to the staggered configuration. This leads to the conclusion that the straight structures are less sensitive to the pseudo-2D effects present, since they are all relatively similar. The relative transverse dispersion does seem to increase as a function of feature size. This could again be the result of enhanced mixing in the wake of the cylinders, leading to increased mass transport in the axial gap between features.

A more thorough fundamental understanding of the pseudo-2D effects in the experimental setup, as well as the observed effects as a function of the porosity of the structure and the dependency on the Péclet number could be obtained from detailed modeling (direct numerical simulations), which is beyond the scope of the current paper. This should include a detailed analysis of the influence of the domain thickness, since it was mentioned that the no-slip z-boundaries on either side of the structure, as well as the tortuous path present in the *z*-direction, may influence the current results. Decoupling of this possible influence from the observed dispersion behavior will yield values for the transverse dispersion coefficient which more accurately describe the actual situation in logpile structures where the fluid is allowed to travel in all directions.

4.5. Correlating the Results

The conclusions regarding the observed trends for a feature size of 1.5 mm allow for an attempt at correlating these results. Such correlations may be used to provide an estimate for the degree of transverse dispersion at various operating conditions in different 3D-printed logpile structures, which can aid in the design of chemical processes employing these structures. Correlations are fitted based on eq 12. By multivariate optimization, using the porosity of the structure, the feature size, hydraulic diameter, and Péclet number, the correlations in eqs 16 and 17 were obtained for the staggered and straight configurations, respectively. These correlations are plotted alongside the original data in Figures 13 and 14.

$$\frac{D_t}{D_m} = 2.64\frac{1-\epsilon}{\epsilon} + 0.00631\left(\frac{1-\epsilon}{\epsilon}\right)^{2.65}\left(\frac{d_h}{d}Pe_m\right)^{1.67} \tag{16}$$

$$\frac{D_t}{D_m} = 0.769\left(\frac{1-\epsilon}{\epsilon}\right)^{1.31} + 0.0262\epsilon^{2.04}Pe_m^{1.19} \tag{17}$$

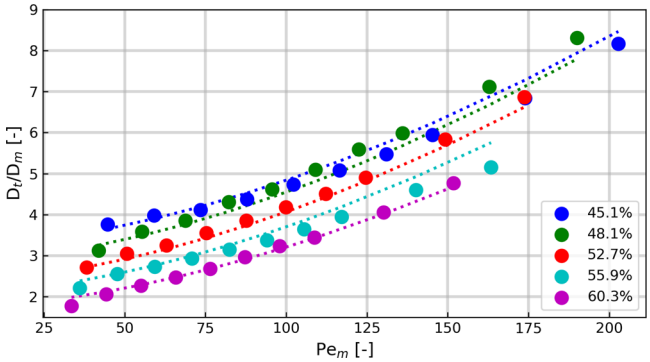

Figure 13. Correlating the relative transverse dispersion in different staggered structures with 1.5 mm feature size and varying porosity. Dots represent experimental data and lines represent the correlation in eq 16.

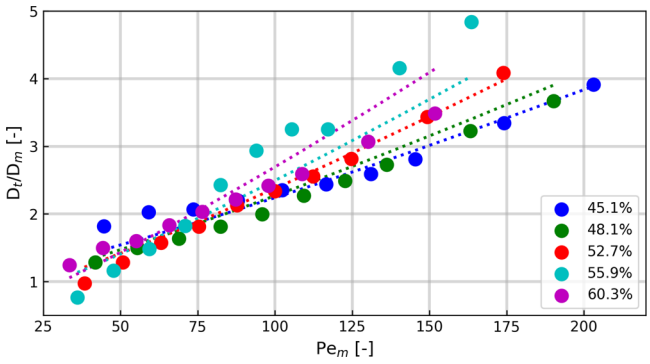

Figure 14. Correlating the relative transverse dispersion in different straight structures with 1.5 mm feature size and varying porosity. Dots represent experimental data and lines represent the correlation in eq 17.

For consistency, the staggered configuration data in Figure 13 is plotted as a function of the Péclet number, but it was observed that the data are better correlated through a modified Péclet number, using the hydraulic diameter (the aperture between features) as characteristic length. The fitted coefficients were obtained after optimization, resulting in a MAPE of 3.74%. Both this low MAPE and the visual comparison in Figure 13 confirm that this correlation, and particularly the use of the modified Péclet number, provides a good description of the experimental data.

The optimized correlation for the straight configuration has a MAPE of 9.26%. This seems high, but should be put in perspective with consideration of the high coefficient of variation of the data.

https://doi.org/10.1021/acsengineeringau.1c00040
ACS Eng. Au 2022, 2, 236−247

Both fitted correlations have a slope that is lower compared to the correlation for the randomly packed bed of spheres (which is shown in Figure 7), meaning that a change in Péclet number will influence the transverse dispersion to a lesser degree. Similar observations with quantitatively comparable differences in transverse dispersion coefficient have been made in the literature for comparisons between ordered (e.g., face-centered cubic) and randomly packed beds of spheres.[44] The observed effects can be attributed to an inherent difference between randomly packed beds and ordered structures.[45] Because of the periodic nature of ordered structures, streamlines are symmetric throughout the structure and will not cross over into another repeating unit. Transverse dispersion is thus ultimately limited by a diffusion process as only diffusion between adjacent streamlines allows for mass transport between repeating units.[36,46] This contrasts with randomly packed beds, in which the asymmetric structure and the broader tortuosity distribution resulting from this causes the streamlines to be more randomly distributed, increasing the apparent transverse dispersion due to transverse convection beyond the scale of a periodically repeating unit in a logpile structure.[47]

5. CONCLUSIONS

The transverse dispersion behavior of 3D-printed logpile structures was quantified for the first time using a novel measurement technique employing infrared absorption to visualize the flow of tracer gas. The measurements of 22 structural variations at different superficial velocities have confirmed that the transverse dispersion in staggered logpile structures is indeed significantly higher than in straight logpile structures, and that the transverse dispersion can indeed be tailored by changing the design of the structure, namely, feature size and porosity. This, in addition to the tunability of catalyst holdup and fluid−solid interfacial area, allows for relatively broad windows of reactor operation. This contrasts with structures with a straight configuration, the channeled internals of which limit the range of transverse dispersion coefficients that can be achieved. The transverse dispersion behavior was correlated to operating conditions (Péclet number) and the geometry of the structure (feature size, hydraulic diameter, and porosity), and the proposed correlations aid to estimate the extent of lateral dispersion in logpile structures to facilitate reactor design. Additional modeling work is required to fully understand the influence of the structural parameters and come to a more fundamental explanation of the relevant phenomena rather than a descriptive correlation.

AUTHOR INFORMATION

Corresponding Author

Martin van Sint Annaland − *Department of Chemical Engineering and Chemistry, Eindhoven University of Technology, Eindhoven 5600MB, The Netherlands;* orcid.org/0000-0002-2903-7443; Email: M.v.SintAnnaland@tue.nl

Authors

Leon R.S. Rosseau − *Department of Chemical Engineering and Chemistry, Eindhoven University of Technology, Eindhoven 5600MB, The Netherlands;* orcid.org/0000-0002-5691-1677

Merlijn A.M.R. Schinkel − *Department of Chemical Engineering and Chemistry, Eindhoven University of Technology, Eindhoven 5600MB, The Netherlands*

Ivo Roghair − *Department of Chemical Engineering and Chemistry, Eindhoven University of Technology, Eindhoven 5600MB, The Netherlands*

Complete contact information is available at: https://pubs.acs.org/10.1021/acsengineeringau.1c00040

Notes

The authors declare no competing financial interest.

ACKNOWLEDGMENTS

This article is based on research undertaken in relation to a project (ZEOCAT-3D) which has received funding from the European Union's Horizon 2020 research and innovation program, under Grant Agreement No. 814548. The authors would like to thank the EU Horizon 2020 program for this opportunity. This publication only reflects the author's views and neither the funding Agency nor the European Commission are responsible for any use that may be made of the information contained therein.

NOMENCLATURE

A	Absorbance, -
C	Concentration, mol m^{-3}
D	Dispersion coefficient, m^2 s^{-1}
d	Diameter of printed features, m
d_h	Hydraulic diameter, m
I	Intensity, -
L	Half column width, m
N	Number of data points, -
n	Counting variable, -
Pe	Péclet number, -
Re	Reynolds number, -
Sc	Schmidt number, -
T	Transmission, -
t	Time s
U	Superficial velocity, m s^{-1}
$\mathbf{u}$	Velocity vector, m s^{-1}
u	Interstitial velocity, m s^{-1}
x	Axial coordinate, m
y	Transverse coordinate, m
α	Fitted coefficient, -
β	Fitted coefficient, -
γ	Fitted coefficient, -
Δy	Half injector width, m
ϵ	Porosity, -
σ	Standard deviation, m
τ	Tortuosity, -

Subscripts

0	Reference
m	Molecular
PB	Packed bed
t	Transverse

REFERENCES

(1) Akhtar, F.; Andersson, L.; Ogunwumi, S.; Hedin, N.; Bergström, L. Structuring adsorbents and catalysts by processing of porous powders. *J. Eur. Ceram. Soc.* **2014**, *34*, 1643−1666.

(2) Gascon, J.; Van Ommen, J. R.; Moulijn, J. A.; Kapteijn, F. Structuring catalyst and reactor - An inviting avenue to process intensification. *Catal. Sci. Technol.* **2015**, *5*, 807−817.
(3) Kraushaar-Czarnetzki, B., Peter Müller, S. In *Synthesis of Solid Catalysts*; De Jong, K. P., Ed.; Wiley-VCH Verlag GmbH & Co. KGaA: Weinheim, Germany, 2009; pp 173−199.
(4) Kapteijn, F.; Moulijn, J. A. Structured catalysts and reactors − Perspectives for demanding applications. *Catal. Today* **2020**, *383*, 5−14.
(5) Rezaei, F.; Webley, P. Structured adsorbents in gas separation processes. *Sep. Purif. Technol.* **2010**, *70*, 243−256.
(6) Vervloet, D.; Kapteijn, F.; Nijenhuis, J.; Van Ommen, J. R. Process intensification of tubular reactors: Considerations on catalyst hold-up of structured packings. *Catal. Today* **2013**, *216*, 111−116.
(7) Zocca, A.; Colombo, P.; Gomes, C. M.; Günster, J. Additive Manufacturing of Ceramics: Issues, Potentialities, and Opportunities. *J. Am. Ceram. Soc.* **2015**, *98*, 1983−2001.
(8) Chen, Z.; Li, Z.; Li, J.; Liu, C.; Lao, C.; Fu, Y.; Liu, C.; Li, Y.; Wang, P.; He, Y. 3D printing of ceramics: A review. *J. Eur. Ceram. Soc.* **2019**, *39*, 661−687.
(9) Travitzky, N.; Bonet, A.; Dermeik, B.; Fey, T.; Filbert-Demut, I.; Schlier, L.; Schlordt, T.; Greil, P. Additive manufacturing of ceramic-based materials. *Adv. Eng. Mater.* **2014**, *16*, 729−754.
(10) Hurt, C.; Brandt, M.; Priya, S. S.; Bhatelia, T.; Patel, J.; Selvakannan, P. R.; Bhargava, S. Combining additive manufacturing and catalysis: A review. *Catal. Sci. Technol.* **2017**, *7*, 3421−3439.
(11) Rosseau, L. R. S.; Middelkoop, V.; Willemsen, H. A. M.; Roghair, I.; van Sint Annaland, M. Review on additive manufacturing of catalysts and sorbents and the potential for process intensification. *Front. Chem. Eng.* **2022**, *4*, 834547.
(12) Lewis, J. A.; Smay, J. E.; Stuecker, J.; Cesarano, J. Direct ink writing of three-dimensional ceramic structures. *J. Am. Ceram. Soc.* **2006**, *89*, 3599−3609.
(13) Faes, M.; Valkenaers, H.; Vogeler, F.; Vleugels, J.; Ferraris, E. Extrusion-based 3D printing of ceramic components. *Procedia CIRP* **2015**, *28*, 76−81.
(14) Lefevere, J.; Mullens, S.; Meynen, V. The impact of formulation and 3D-printing on the catalytic properties of ZSM-5 zeolite. *Chem. Eng. J.* **2018**, *349*, 260−268.
(15) Lefevere, J.; Protasova, L.; Mullens, S.; Meynen, V. 3D-printing of hierarchical porous ZSM-5: The importance of the binder system. *Mater. Des.* **2017**, *134*, 331−341.
(16) M'Barki, A.; Bocquet, L.; Stevenson, A. Linking Rheology and Printability for Dense and Strong Ceramics by Direct Ink Writing. *Sci. Rep.* **2017**, *7*, 1−10.
(17) Tomašić, V.; Jović, F. State-of-the-art in the monolithic catalysts/reactors. *Appl. Catal. Gen.* **2006**, *311*, 112−121.
(18) Lerou, J. J.; Froment, G. F. Velocity, temperature and conversion profiles in fixed bed catalytic reactors. *Chem. Eng. Sci.* **1977**, *32*, 853−861.
(19) Shinnar, R.; Doyle, F. J.; Budman, H. M.; Morari, M. Design considerations for tubular reactors with highly exothermic reactions. *AIChE J.* **1992**, *38*, 1729−1743.
(20) Delgado, J. M. P. Q. A critical review of dispersion in packed beds. *Heat Mass Transfer* **2006**, *42*, 279−310.
(21) Delgado, J. M. P. Q.; Guedes de Carvalho, J. R. F. Measurement of the Coefficient of Transverse Dispersion in Flow Through Packed Beds for a Wide Range of Values of the Schmidt Number. *Transp. Porous Media* **2001**, *44*, 165−180.
(22) Amin, M. H. G.; Glbbs, S. J.; Chorley, R. J.; Richards, K. S.; Carpenter, T. A.; Hall, L. D. Study of flow and hydrodynamic dispersion in a porous medium using pulsed-field-gradient magnetic resonance. *Proc. R. Soc. A: Math. Phys. Eng. Sci.* **1997**, *453*, 489−513.
(23) Manz, B.; Alexander, P.; Gladden, L. F. Correlations between dispersion and structure in porous media probed by nuclear magnetic resonance. *Phys. Fluids* **1999**, *11*, 259.
(24) Dixon, A. G.; Medeiros, N. J. Computational Fluid Dynamics Simulations of Gas-Phase Radial Dispersion in Fixed Beds with Wall Effects. *Fluids* **2017**, *2*, 56.
(25) Chandra, V.; Das, S.; Peters, E. A. J. F.; Kuipers, J. A. M. Direct numerical simulation of hydrodynamic dispersion in open-cell solid foams. *Chem. Eng. J.* **2019**, *358*, 1305−1323.
(26) Dang, T. Y.; Kolkman, T.; Gallucci, F.; van Sint Annaland, M. Development of a novel infrared technique for instantaneous, whole-field, non invasive gas concentration measurements in gas-solid fluidized beds. *Chem. Eng. J.* **2013**, *219*, 545−557.
(27) Medrano, J. A.; De Nooijer, N. C. A.; Gallucci, F.; Van Sint Annaland, M. Advancement of an Infra-Red Technique for Whole-Field Concentration Measurements in Fluidized Beds. *Sensors* **2016**, *16*, 1−18.
(28) Vollmer, M.; Mollmann, K.-P. *Infrared Thermal Imaging: Fundamentals, Research and Applications*; Wiley-VCH Verlag GmbH & Co. KGaA: Weinheim, Germany, 2010.
(29) Ngo, T. D.; Kashani, A.; Imbalzano, G.; Nguyen, K. T.; Hui, D. Additive manufacturing (3D printing): A review of materials, methods, applications and challenges. *Compos. B Eng.* **2018**, *143*, 172−196.
(30) Guo, N.; Leu, M. C. Additive manufacturing: Technology, applications and research needs. *Front. Mech. Eng.* **2013**, *8*, 215−243.
(31) Yuniarto, K.; Aris Purwanto, Y.; Purwanto, S.; Welt, B. A.; Karia Purwadaria, H.; Candra Sunarti, T. Infrared and Raman studies on polylactide acid and polyethylene glycol-400 blend. *AIP Conf. Proc.* **2015**, 20101.
(32) Alsoufi, M. S.; Alhazmi, M. W.; Suker, D. K.; Yunus, M.; Malibari, R. O. From 3D models to FDM 3D prints: experimental study of chemical treatment to reduce stairs-stepping of semi-sphere profile. *AIMS Mater. Sci.* **2019**, *6*, 1086−1106.
(33) Peng, E.; Zhang, D.; Ding, J. Ceramic Robocasting: Recent Achievements, Potential, and Future Developments. *Adv. Mater.* **2018**, *30*, 1802404.
(34) Claessens, B.; Dubois, N.; Lefevere, J.; Mullens, S.; Cousin-Saint-Remi, J.; Denayer, J. 3D-Printed ZIF-8 Monoliths for Biobutanol Recovery. *Ind. Eng. Chem. Res.* **2020**, *59*, 8813−8824.
(35) Crank, J. *The Mathematics of Diffusion*; Oxford University Press: Oxford, 1975.
(36) Daneyko, A.; Hlushkou, D.; Khirevich, S.; Tallarek, U. From random sphere packings to regular pillar arrays: Analysis of transverse dispersion. *J. Chromatogr. A* **2012**, *1257*, 98−115.
(37) Delgado, J. M. P. Q. Longitudinal and transverse dispersion in porous media. *Chem. Eng. Res. Des.* **2007**, *85*, 1245−1252.
(38) Gunn, D. J. Axial and radial dispersion in fixed beds. *Chem. Eng. Sci.* **1987**, *42*, 363−373.
(39) Bischoff, K. B. A note on gas dispersion in packed beds. *Chem. Eng. Sci.* **1969**, *24*, 607.
(40) Wakeham, W. A.; Slater, D. H. Diffusion coefficients for n-alkanes in binary gaseous mixtures with nitrogen. *J. Phys. B: Atom. Mol. Phys.* **1973**, *6*, 886−896.
(41) Jacobs, T.; Peeters, L.; Vermant, J. Binary Diffusion Coefficients of Lower Alkanes in Nitrogen and Argon. *Bull. Soc. Chim. Belg.* **1970**, *79*, 337−341.
(42) Matsunaga, N.; Hori, M.; Nagashima, A. Gaseous Diffusion Coefficients of Propane and Propylene into Air, Nitrogen and Oxygen. *Netsu Bussei* **2007**, *21*, 143−148.
(43) Coelho, M. A. N.; Guedes de Carvalho, J. R. F. Transverse dispersion in granular beds. I: Mass transfer from a wall and the dispersion coefficient in packed beds. *Chem. Eng. Res. Des.* **1988**, *66*, 165−177.
(44) Hlushkou, D.; Piatrusha, S.; Tallarek, U. Impact of diffusion on transverse dispersion in two-dimensional ordered and random porous media. *Phys. Rev. E* **2017**, *95*, 063108.
(45) Koch, D. L.; Cox, D. G.; Brenner, H.; Brady, J. F. The effect of order on dispersion in porous media. *J. Fluid Mech.* **1989**, *200*, 173−188.
(46) Daneyko, A.; Khirevich, S.; Höltzel, A.; Seidel-Morgenstern, A.; Tallarek, U. From random sphere packings to regular pillar arrays: Effect of the macroscopic confinement on hydrodynamic dispersion. *J. Chromatogr. A* **2011**, *1218*, 8231−8248.

https://doi.org/10.1021/acsengineeringau.1c00040
ACS Eng. Au 2022, 2, 236−247

(47) Ahmadi, S.; Sefidvash, F. Study of Pressure Drop in Fixed Bed Reactor Using a Computational Fluid Dynamics (CFD) Code. *ChemEngineering* **2018**, *2*, 14.

https://doi.org/10.1021/acsengineeringau.1c00040
ACS Eng. Au 2022, 2, 236−247